



Short note

An extension of high-order shock-fitted detonation propagation in explosives

Christopher M. Romick^{a,*}, Tariq D. Aslam^b^a Eureka Physics LLC, Washington, DC 20006, USA^b Theoretical Division, Physics and Chemistry of Materials (T-1), Los Alamos National Laboratory, Los Alamos, NM 87545, USA

ARTICLE INFO

Article history:

Received 29 November 2018

Received in revised form 24 May 2019

Accepted 6 June 2019

Available online 7 June 2019

Keywords:

Numerical methods

Shock-fitting

Detonation

High explosives

ABSTRACT

An update to the numerical shock-fitting scheme from [1] is proposed. The updated scheme locally lowers the order of the scheme in the region of secondary non-fitted waves that interact with the fitted front. In addition, it utilizes a non-uniform mapping from the physical space to the computational space along the streamline direction to offer computational savings over the use of an uniform spacing. The utility of the scheme is first demonstrated on planar ideal gas detonating flows. It is then applied to detonation propagation in a two-dimensional axisymmetric geometry while utilizing an Arrhenius Wescott-Stewart-Davis model for PBX 9502.

© 2019 Elsevier Inc. All rights reserved.

1. Introduction

A detonation is a complex wave consisting of a leading shock with attached reaction wave that drives the flow [2]. The modeling of such phenomena propagating in high explosives (HE) has a long history and is often computationally expensive when reactive flow is used. In fact, it was demonstrated that for shock-capturing, when utilizing a combined essentially non-oscillatory (ENO) and Lax–Friedrichs (LF) scheme, a minimum of 50 points in the reaction zone were needed in order to obtain $\mathcal{O}(50 \text{ m/s})$ error in the detonation phase speed [3]. Moreover, insensitive HEs (IHE), like PBX 9502, which have improved safety characteristics [4], exhibit longer reaction zones than conventional HEs. As these IHEs mostly retain the finer reaction length scales as well, the computational expense to accurately predict the speed and pressure of the detonation wave is increased yet further.

Further compounding the complexity and cost of reactive modeling of detonation propagation in HEs is the use of shock state dependency (or related to this, the entropy of the reactants) in many of the constructions, e.g. WSD [5], SURF [6], CREST [7]. Due to the ease of use, it is common practice to use shock-capturing, which utilizes an inherent numerical viscosity to smoothen the shock at the expense of thickening it. This introduces ambiguity to what the actual shock state is. The shock-fitting approach allows for this ambiguity to be removed. Therefore, it restores the chance of obtaining a highly accurate solution on either side of the fitted shock as well as for the location of the shock.

The objective of this short note is to present an updated shock-fitting method that can be applied to a wider set of problems than previously shown in [1] while retaining the possibility of providing highly accurate predictions of detonation propagation in HEs. This is accomplished by addressing the issue of algorithmic failure of shock-fitting when non-fitted secondary waves interact with the fitted front. First, the pertinent governing equations are very briefly reviewed. This is

* Corresponding author.

E-mail address: christopher.romick@gmail.com (C.M. Romick).

followed by the updates to the computational algorithm. Last, the algorithm is applied to two representative examples: planar ideal gas detonation waves and unconfined charges of PBX 9502 using a modified Wescott-Scott-Davis (WSD) model.

2. Governing equations

For brevity of the note only a short introduction to the governing equations is given here; however, the full development of the governing equations is detailed in the original paper [1]. The governing equations utilized in this work are the unsteady, compressible, reactive Euler equations that undergo a single irreversible reaction. These equations need to be further supplemented by constitutive relations for both the equation of state (EOS) and the reaction rate which are provided in section 4.

Both slab-type and axisymmetric rate-stick charge geometries can be written into a general form utilizing source terms. After this is transformed for the computational domain, the governing vector equation can be written as

$$\frac{\partial}{\partial \tau} (\sqrt{g} \mathbf{U}) + \frac{\partial \mathbf{f}_\xi}{\partial \xi} + \frac{\partial \mathbf{f}_\eta}{\partial \eta} = \sqrt{g} \mathbf{S}, \quad (1)$$

where, g is the determinant of the metric tensor of the shock-fitted coordinates, \mathbf{U} the physical space evolved state variables, \mathbf{f}_ξ and \mathbf{f}_η the ξ and η directional fluxes respectively, and \mathbf{S} the source terms from the physical space equations. In this computational space, the set of evolved quantities are $\sqrt{g} \mathbf{U}$.

3. Numerical implementation

The nominally fifth-order, method of lines approach detailed in [1] which was based on the work of [8], remains the basis of this updated, more robust shock-fitting algorithm. Thus, only the alterations from the algorithm of [1] will be detailed here. There are only a few of modifications to the previous algorithm: 1) the explicit evolution of the normal shock speed, D_N , 2) the addition of a switch for dealing with wave interactions near the front, and 3) a modification to the relationship between z and η .

3.1. Evolution of the shock speed

In [1], the normal shock speed was calculated using the jump conditions since the state values at the front were evolved in time. However, in the present algorithm the normal shock speed is evolved in time. This is commonly referred to as a shock change equation and can take various different forms which are mathematically equivalent. The approach for the shock change equation taken here is similar to that of [9]; however, it utilizes the total energy flux at the front (multiplied by the geometric mapping term \sqrt{g}) in place of the momentum flux

$$\frac{dD_N}{d\tau} = \left[\frac{d(\sqrt{g} E_t|_s)}{dD_N} \right]^{-1} \frac{\partial}{\partial \tau} (\sqrt{g} E_t) \Big|_s, \quad (2)$$

where the subscript s denotes the evaluation at the front. One reason the rate of change of the total energy was used in this work is that it incorporates changes in both momentum fluxes as well as internal energy. Equation (2) thus relates the shock acceleration to the flux at the front.

In general, the total energy at the front, is a complex, implicit function of the normal shock speed due to the EOS. Therefore, an approximation of $d(\sqrt{g} E_t|_s)/dD_N$ is needed. This approximation is calculated using a centered fourth-order finite difference scheme:

$$\frac{d(\sqrt{g} E_t|_s)}{dD_N} = \sqrt{g_s} \frac{d(E_t|_s)}{dD_N} \approx \left[\sqrt{g_s} \frac{[E_{t_s}(D_{-2}) - 8E_{t_s}(D_{-1}) + 8E_{t_s}(D_{+1}) - E_{t_s}(D_{+2})]}{12\Delta D_N} \right]^{-1}, \quad (3)$$

where E_{t_s} is the total energy after the shock,

$$D_{-2} = (1 - 2\Delta)D_N, \quad D_{-1} = (1 - \Delta)D_N, \quad D_{+1} = (1 + \Delta)D_N, \quad D_{+2} = (1 + 2\Delta)D_N,$$

and Δ is a dimensionless spacing in the normal shock speed space (in this work $\Delta = 10^{-4}$). Again following the approach of [9], the $\partial(\sqrt{g} E_t)/\partial \tau|_s$ term is obtained from the fourth component of the governing equation, Eqn. (1), evaluated at the shock front utilizing the fluxes.

3.2. Robustness factor

The current algorithm continues to utilize a combined LF and fifth-order mapped weighted essentially non-oscillatory (WENO5M) scheme for calculating flux derivatives at internal nodes. This WENO5M-LF scheme works well including for

capturing discontinuities; however, it requires several nodal values on either side of the node being evaluated meaning that this method can not be used near the front. Therefore, in the algorithm from [1], simple high-order, skewed finite differences based on Taylor series expansions were used for approximating the η flux derivatives near the front. This can be problematic though when a secondary (non-fitted) discontinuity from the interior approaches the front, routinely ruining the calculation and causing it to end prematurely. Since in some cases complex waves patterns exist, it is useful to have a fitting method that maintains the nominal accuracy when the flow is smooth but has enhanced overall stability. In this section, the current implementation of this methodology is presented.

The current technique utilizes a convex, weighted combination of the highly accurate, high-order scheme and a more robust low-order scheme (which will be denoted with subscripts h and l respectively in this section) at the front and the near region ($N_\eta - 2$, $N_\eta - 1$, and N_η) where the high-order skewed finite differences are utilized. For any representative component, $\partial f_\eta / \partial \eta$, of the vector flux derivative, $\partial \mathbf{f}_\eta / \partial \eta$, from Eqn. (1), the current approach can be written as

$$\begin{aligned} \frac{\partial f_\eta}{\partial \eta} &= (1 - \delta) \left(\hat{f}'_h + \mathcal{O}(\Delta \eta^h) \right) + \delta \left(\hat{f}'_l + \mathcal{O}(\Delta \eta^l) \right) \\ &= (1 - \delta) \hat{f}'_h + \delta \hat{f}'_l + \left[\mathcal{O}(\Delta \eta^h) - \delta \mathcal{O}(\Delta \eta^h) + \delta \mathcal{O}(\Delta \eta^l) \right], \end{aligned} \quad (4)$$

where δ is the weight given to low-order scheme approximation (also referred to here as the robustness switch factor), \hat{f}'_h the high-order skewed finite difference approximation and \hat{f}'_l the low-order approximation with the associated truncation errors being $\mathcal{O}(\Delta \eta^h)$ and $\mathcal{O}(\Delta \eta^l)$, respectively.

Equation (4) is a linear function in δ which transitions from the high-order scheme (at $\delta = 0$) to the low-order robust scheme (at $\delta = 1$). In addition, it is clear that the size of δ determines the size of the truncation error of the overall approximation. The aim of this weighting is to maintain high accuracy when the flow is smooth; therefore, δ must be at least or smaller than $\mathcal{O}(\Delta \eta^{(h-l)})$ when the flow is smooth to maintain a truncation error of high-order. Consistent with the previous fitting algorithm, the high-order approximations utilized in this work are

$$\hat{f}'_h|_{N_\eta-2} = \frac{1}{12\Delta\eta} \left(f_\eta|_{N_\eta-4} - 8 f_\eta|_{N_\eta-3} + 8 f_\eta|_{N_\eta-1} - f_\eta|_{N_\eta} \right), \quad (5)$$

$$\hat{f}'_h|_{N_\eta-1} = \frac{1}{12\Delta\eta} \left(-f_\eta|_{N_\eta-4} + 6 f_\eta|_{N_\eta-3} - 18 f_\eta|_{N_\eta-2} + 10 f_\eta|_{N_\eta-1} + 3 f_\eta|_{N_\eta} \right), \quad (6)$$

$$\hat{f}'_h|_{N_\eta} = \frac{1}{60\Delta\eta} \left(-12 f_\eta|_{N_\eta-5} + 75 f_\eta|_{N_\eta-4} - 200 f_\eta|_{N_\eta-3} + 300 f_\eta|_{N_\eta-2} - 300 f_\eta|_{N_\eta-1} + 137 f_\eta|_{N_\eta} \right). \quad (7)$$

The use of the fourth-order stencils in Eqns. (5)–(6) alongside the fifth-order finite difference of Eqn. (7) helps ensure numerical stability when $\delta \equiv 0$. However, as demonstrated in [1,9] for similar algorithms with the equivalent of $\delta \equiv 0$, the use of such stencils does not preclude the algorithm from retaining its global fifth-order convergence rate for smooth flows.

Since the high-order scheme utilized is nominally fifth-order and the simplest, most robust schemes are usually highly dissipative first-order schemes, δ must be $\mathcal{O}(\Delta \eta^4)$ for smooth flow. As there is only information available for the approximation behind the front, a simple standard first-order, one-sided finite difference scheme is used at the front, N_η . At the following nodes, $N_\eta - 2$ and $N_\eta - 1$, information exists on either side of the node; thus, a first-order LF scheme is utilized. To obtain a δ that is $\mathcal{O}(\Delta \eta^4)$ for smooth flow, a logical approach would be to compare the fourth- and fifth-order finite difference approximations for the gradient in the evolved variable, w , in the η direction:

$$\delta_{45}|_j = [\hat{w}'_5 - \hat{w}'_4]_j \quad \text{for } N_\eta - 2 \leq j \leq N_\eta, \quad (8)$$

where the fifth-order approximations are given by

$$\begin{aligned} \hat{w}'_5|_{N_\eta-2} &= \frac{-3w_{N_\eta} + 30w_{N_\eta-1} + 20w_{N_\eta-2} - 60w_{N_\eta-3} + 15w_{N_\eta-4} - 2w_{N_\eta-5}}{60\Delta\eta}, \\ \hat{w}'_5|_{N_\eta-1} &= \frac{12w_{N_\eta} + 65w_{N_\eta-1} - 120w_{N_\eta-2} + 60w_{N_\eta-3} - 20w_{N_\eta-4} + 3w_{N_\eta-5}}{60\Delta\eta}, \\ \hat{w}'_5|_{N_\eta} &= \frac{137w_{N_\eta} - 300w_{N_\eta-1} + 300w_{N_\eta-2} - 200w_{N_\eta-3} + 75w_{N_\eta-4} - 12w_{N_\eta-5}}{60\Delta\eta}, \end{aligned}$$

and the fourth-order approximations are given by

$$\begin{aligned} \hat{w}'_4|_{N_\eta-2} &= \frac{-w_{N_\eta} + 8w_{N_\eta-1} - 8w_{N_\eta-3} + w_{N_\eta-4}}{12\Delta\eta}, \\ \hat{w}'_4|_{N_\eta-1} &= \frac{-w_{N_\eta} + 6w_{N_\eta-1} - 18w_{N_\eta-2} + 10w_{N_\eta-3} + 3w_{N_\eta-4}}{12\Delta\eta}, \end{aligned}$$

$$\hat{w}'_4|_{N_\eta} = \frac{25w_{N_\eta} - 48w_{N_\eta-1} + 36w_{N_\eta-2} - 16w_{N_\eta-3} + 3w_{N_\eta-4}}{12\Delta\eta}.$$

Equations (8) are $\mathcal{O}(\Delta\eta^4)$ in smooth flow; thus, accomplishing the first goal for the desired robustness switch weighting. However, δ_{45} can be quite large for non-smooth flow e.g. a non-fitted discontinuity; moreover, it is not dimensionless, which is also a desired property. By choosing to scale the square of δ_{45} in the following manner, a dimensionless factor that at most approaches unity for non-smooth flow is obtained:

$$\delta_s|_j = \frac{(\hat{w}'_5 - \hat{w}'_4)^2}{(\hat{w}'_5)^2 + (\hat{w}'_4)^2 + 2|\hat{w}'_4\hat{w}'_5| + \epsilon}|_j \quad \text{for } N_\eta - 2 \leq j \leq N_\eta. \quad (9)$$

Here, $\epsilon = 1 \times 10^{-20}$ and is included to ensure that one does not divide by zero. The square, as opposed to the magnitude, has been chosen as it is more continuous when the fourth- and fifth-order approximations are opposite signs; furthermore, this scaling yields a result that is invariant to the size of the discrete jump. In addition, it should be noted that Eqns. (9) are $\mathcal{O}(\Delta\eta^8)$ in smooth flow.

This scaling is still however affected by the location of such a discrete jump. In order to correct for this issue, the local robustness factor is rescaled by the minimum value of δ_s when there is a discrete jump present within the stencil and limited to a maximum value of unity:

$$\delta_l|_{N_\eta-2} = \min\left(1, \frac{961}{16}\delta_s|_{N_\eta-2}\right), \quad \delta_l|_{N_\eta-1} = \min\left(1, \frac{5041}{36}\delta_s|_{N_\eta-1}\right), \quad \delta_l|_{N_\eta} = \min\left(1, \frac{17161}{36}\delta_s|_{N_\eta}\right). \quad (10)$$

The overall weight, δ , is then calculated as a simple average of the local values over the nodes near the front:

$$\delta = \frac{\delta_l|_{N_\eta-2} + \delta_l|_{N_\eta-1} + \delta_l|_{N_\eta}}{3}. \quad (11)$$

The use of such a weighting function adds stability to the scheme to handle the complexity of secondary wave patterns at the expense lowering the accuracy of the overall scheme locally. However, when the flow is smooth the algorithm still utilizes the highly accurate, high-order scheme. It should be noted that while the highly-accurate scheme is retained in areas of smooth flow, the utilization of the lower-order schemes (near the material interfaces in the ξ direction or those necessary to capture the interaction of secondary waves with the fitted front) as mentioned in the previous article likely cause the overall convergence rate of the scheme to deteriorate to near first order.

3.3. Non-uniform spatial discretization

The transformation utilized in this work also deviates slightly from that in [1]. A non-uniform mapping between η and z is introduced here. As the applications for this algorithm require significant resolution near the front within the early reaction zone and less resolution further from the front, it is advantageous for the mapping to increase the spacing between nodal points in the physical space (z) while maintaining a uniform spacing in the computational space (η). This further reduces the computational cost of studying shock-fitted flows at longer times and domains.

In the current work, this is accomplished using a combination of a linear function and a natural logarithm of hyperbolic cosine functions:

$$z(\xi, \eta, \tau) = z_s(\xi, \tau) + \frac{1}{2} \left((c+2)\eta + \frac{c}{a} \ln \left(\frac{\cosh(ab)}{\cosh(a(\eta-b))} \right) \right), \quad (12)$$

where $z_s(\xi, \tau)$ is the shock locus, c the increase in the scale, a sets the rate of the transition and b sets the center of the transition. This choice yields a smooth and simple function for the metric, $\partial z / \partial \eta$:

$$\frac{\partial z}{\partial \eta} = \frac{1}{2} ((c+2) - c \tanh(a(\eta-b))) = 1 + \frac{c}{2} [1 - \tanh(a(\eta-b))]. \quad (13)$$

From Eqn. (13), it is clear as c approaches 0 that one recovers a uniform spacing in the physical grid that is shock-attached. However, it may be less clear that $c = 1$ results in the doubling of the original spacing; likewise, $c = 3$ results in the quadrupling of the original spacing. The choices for the rate and location of the transition are problem dependent and must be carefully chosen. Selection too close to the front will sacrifice too much accuracy for the computational savings gained. This is clearly demonstrated in section 4.2.

4. Applications

To demonstrate the important features of the current shock-fitting method, several problems are examined. The first case examined is planar detonations in ideal gases. This case verifies the rate of convergence for smooth flow behind the fitted front; in addition, it demonstrates the ability of the algorithm to switch to the lower-order stencil in non-smooth

Table 1

Late time error in detonation velocity and rate of convergence for a stable, steadily propagating detonation in a mixture of CPIGs.

$\Delta\eta$	Late time error in D_N/D_{CJ}	r_c
0.10000	1.40×10^{-6}	—
0.05000	2.16×10^{-7}	2.70
0.02500	7.57×10^{-9}	4.84
0.01250	2.33×10^{-10}	5.02
0.00625	7.13×10^{-12}	5.03

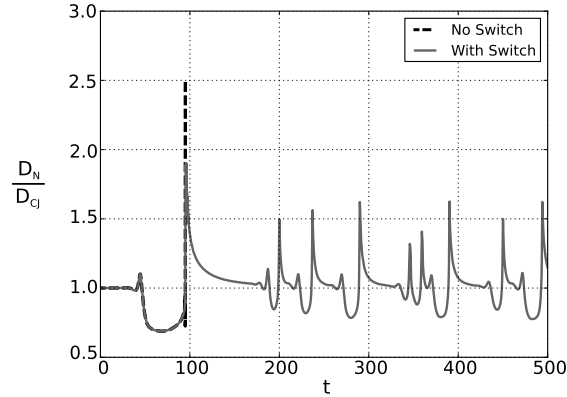


Fig. 1. Scaled detonation speed versus time curves for the detonation with $E = 31$.

flow to handle strong, secondary, overtaking shocks. The second case is a HE rate-stick charge and is used to demonstrate the computational savings over an uniform mapping and the possible pitfalls of the non-uniform mapping. Both cases presented are initialized using the planar Zel'dovich-von Neumann-Döring (ZND) profile for a detonation traveling at the Chapman-Jouguet (CJ) detonation speed, D_{CJ} .

4.1. Planar detonation wave

The propagation of planar (one-dimensional) detonations in a mixture of calorically perfect ideal gases (CPIG) with one-step irreversible kinetics have been studied extensively [9–12]. The constitutive relations for the EOS and reaction rate for a mixture of CPIGs that undergo a single irreversible reaction are

$$e = \frac{p}{(\gamma - 1)\rho} - \lambda q, \quad (14)$$

$$R = k(1 - \lambda) \exp\left(\frac{-\rho E}{p}\right), \quad (15)$$

where e is the specific internal energy, p the pressure, γ the adiabatic exponent, ρ the density, λ the reaction progress variable, q the heat release of the reaction, R the reaction rate, k the reaction rate constant and E the activation energy. Equation (14) is more generally the EOS for a mixture of polytropic fluids with a constant adiabatic exponent and is representative of a mixture of CPIGs for $1 \leq \gamma \leq 5/3$. The standard non-dimensional parameters for this model are an ambient density of $\rho_0 = 1$, an ambient pressure of $p_0 = 1$, a heat release of reaction of $q = 50$, and a constant adiabatic exponent of $\gamma = 1.2$, which yield $D_{CJ} \approx 6.80947463$. In addition, the half-reaction zone length, which is the distance from the shock front to the point where $\lambda = 1/2$ for the steady ZND profile, is $L_{1/2} = 1$.

In order to first establish the convergence rate of the algorithm for smooth flow, a stable case is examined ($E = 25$). Table 1 shows the error in the predicted late time detonation velocity as well as the rate of convergence of the algorithm. This demonstrates that when the new algorithm is applied to the smooth flow region behind the fitted-shock where no strong shocks are captured, that one still recovers the nominal fifth-order convergence rate.

For large activation energies, this model undergoes a transition into more chaotic like behavior with the reaction wave detaching from the leading shock and eventually giving rise to strong secondary non-fitted shocks. These non-fitted shocks ultimately catch the leading fitted shock and cause a failure of the algorithm without the robustness switch. Fig. 1 is a time-history for the detonation speed scaled by the CJ speed of such an unstable detonation ($E = 31$). It contains two curves; the solid curve is that of the current, more robust algorithm, which can handle the interaction between the strong secondary non-fitted shock and the leading fitted shock, and the dashed curve is for the algorithm without the switch. The trace for the case without the robustness switch stops at the point of the interaction between the strong secondary shock

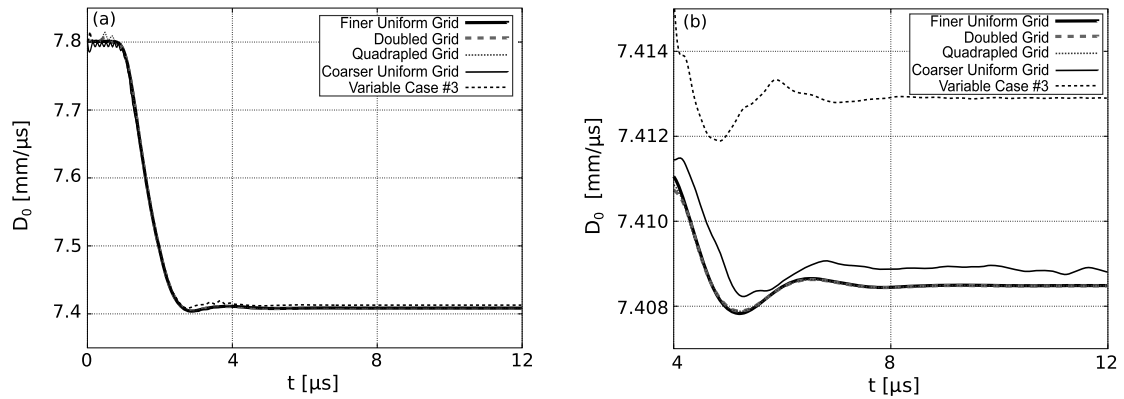


Fig. 2. Detonation phase speed midspan of the charge versus time curves for the AWS model of PBX 9502 in an axisymmetric rate-stick with $r = 4$ mm: (a) complete time-series (b) late time behavior.

with the leading fitted shock as the algorithm fails. It should also be noted that for these type of interactions that a method, such as that of [11], which is purely first-order at the fitted front is likely more robust than the current presented method. However, it is also likely to be much less accurate in areas without these interactions.

4.2. AWS EOS axisymmetric rate-stick

The second application utilizes a set of constitutive relations which are based off the WSD model [5,13] but include an Arrhenius state dependence on the shock temperature. This model is referred to as the AWS model and the parameters utilized in this study, which yield $D_{CJ} \approx 7.801$ mm/μs, can be found in [14], where the model for PBX 9502 was originally introduced. The case examined for this study is an unconfined, axisymmetric rate-stick with a radius of $r = 4$ mm. It should be noted that the main variable of interest is the steady-state phase speed of the detonation and that the material interface follows a prescribed motion for the deflection which is given by

$$\chi_r(\eta, \tau) = \begin{cases} \xi_r - (z - z_s) m \sum_{i=6}^{11} a_i \left(\frac{\tau}{\tau_c} \right)^i & \frac{\tau}{\tau_c} < 1 \\ \xi_r - (z - z_s) m & \frac{\tau}{\tau_c} \geq 1 \end{cases}, \quad (16)$$

where m is the slope corresponding to the deflection angle, a_i the polynomial constants, and τ_c a time constant. Choosing $a_6 = 462$, $a_7 = -1980$, $a_8 = 3465$, $a_9 = -3080$, $a_{10} = 1386$, and $a_{11} = -252$ gives a material interface deflection that is smooth, differentiable in τ , initially parallel to the one-dimensional ZND wave structure, and deflects out to the angle corresponding to an unconfined HE experiment and equivalently, to the maximum streamline deflection of a single oblique shock. This maximum streamline deflection for PBX 9502 corresponds to $\theta_{max} \approx 12.6^\circ$. For this study, the shock-attached domain length is $L_z = 2$ mm, and the time scale for the deflect is $\tau_c = 2$ μs.

Fig. 2 (a) shows the complete time-series for several cases of detonation phase speed mid-span in a PBX 9502 rate-stick charge. The thick solid curve is the time-history for the case where uniform spacing in the physical domain of $\Delta z = 9 \times 10^{-3}$ mm is used; the thin solid curve represents a case where $\Delta z = 18 \times 10^{-3}$ mm. In addition to these two curves, there are three other curves that represent variable resolutions (with a transition rate of $a = 50$): 1) thick dashed curve ($\Delta z_{min} = 9 \times 10^{-3}$ mm, $c = 1$, $b = -0.4$ mm), 2) thin dotted curve ($\Delta z_{min} = 9 \times 10^{-3}$ mm, $c = 3$, $b = -0.4$ mm), and 3) thin dashed curve ($\Delta z_{min} = 9 \times 10^{-3}$ mm, $c = 1$, $b = -0.1$ mm). At early times, *i.e.* before the material interface is fully deflected, the cases with variable resolution clearly deviate from that of the finer uniform resolution case. In fact, there are oscillations around the CJ velocity; these oscillations are likely due to the initial settling of the detonation speed interacting with the variable resolution zone of these simulations. However, they remain less oscillatory than that of the coarser uniform resolution case. From Fig. 2 (a) alone, one can not see a clear discernible difference at later times. The later time behavior of the various cases are demonstrated in Fig. 2 (b). From this, it is clear that the coarser uniform resolution case remains a bit oscillatory even at late times, though variable resolution cases #1 and #2 exhibit the smooth late time behavior of the finer uniform resolution case. However, if the transition occurs too close to the front (variable grid case #3) that the predicted behavior can be remarkably incorrect. This can be clearly seen by examining the late time behavior of third variable resolution case where the predicted steady detonation speed is significantly different from both the fine and coarser uniform resolution cases.

Table 2 demonstrates the speedup for the various cases in comparison from the finer uniform grid case as well as the variable interest, the steady phase speed, D_0 . The variable grid case #1 utilizes 134 nodes in the η direction compared to the 223 nodes of the finer uniform grid case and offers a speedup of 1.7 for a result which is within 0.0001 mm/μs of the original value. Likewise, variable grid case #2 only utilizes 90 nodes and offers a speed-up of 1.9 for a result which is

Table 2
Comparison of uniform and variable grid cases for a PBX 9502 rate stick.

Case	Δz_{min} [mm]	a	b [mm]	c	N_η	D_0 [mm/ μ s]	Speedup
Fine uniform grid	9×10^{-3}	—	—	—	223	7.408486	—
Coarse uniform grid	18×10^{-3}	—	—	—	112	7.408802	3
Variable grid #1	9×10^{-3}	50	−0.4	1	134	7.408478	1.7
Variable grid #2	9×10^{-3}	50	−0.4	3	90	7.408478	1.9
Variable grid #3	9×10^{-3}	50	−0.1	1	117	7.412896	1.8

again within 0.0001 mm/ μ s of the original value. Although this case has less nodes in the η direction, it takes 1.56 times longer than the coarser uniform grid case for the length of the domain chosen. This is due to the smaller time-steps which are required for the finer parts of the grid. However, it recovers the proper behavior of the finer uniform resolution case as opposed to the coarser resolution case. This example clearly demonstrates that a significant speedup can be achieved only as long as the parameters of the transformation are properly chosen.

5. Conclusions

This brief note details the updates to an already highly accurate shock-fitting strategy for examining multi-dimensional shock and detonation flows. The applicability of the present algorithm is extended in comparison with the original, as it is more robust as well as offering computational savings over the original scheme. The ability to treat secondary non-fitted waves which interact with the fitted leading front, as in galloping or cellular detonations, is accomplished through the introduction of a switch which locally lowers the order of the scheme when necessary while maintaining a high-order scheme for smooth flow. Furthermore, the introduction of a non-uniform mapping from the physical space to the computational domain offers a significant speedup for comparable results. This type of speedup could become important if one utilizes shock-fitting in a calibration process for a model. However, the presented updates can carry a major disadvantage, reducing the accuracy of the shock-fitting strategy dramatically such as selecting a non-uniform mapping which transitions discretizations to quickly or in the early reaction zone. Therefore one must utilize a slower transition between discretizations in a region slightly further from the fitted front.

Acknowledgements

The authors would like to thank B.L. Wescott for sharing his wide-ranging EOS code. This study was performed under the auspices of the US Department of Energy. Los Alamos National Laboratory, is managed by Triad National Security, LLC for the U.S. Department of Energy's National Nuclear Security Administration, under contract 89233218CNA000001. The authors also appreciate the useful comments of the referees.

References

- [1] C.M. Romick, T.D. Aslam, High-order shock-fitted detonation propagation in high explosives, *J. Comput. Phys.* 332 (2017) 210–235.
- [2] W. Fickett, W.C. Davis, *Detonation*, University of California, 1979.
- [3] T.D. Aslam, J.B. Bdzil, L.G. Hill, Extension to DSD theory: analysis of PBX 9502 rate stick data, in: *Eleventh Symposium (Intl) on Detonation*, 1998, pp. 21–29.
- [4] B. Dobratz, LLNL explosives handbook: properties of chemical explosives and explosive simulants, Technical Report UCRL-52997, Lawrence Livermore National Laboratory, 1981.
- [5] B.L. Wescott, D.S. Stewart, W.C. Davis, Equation of state and reaction rate for condensed-phase explosives, *J. Appl. Phys.* 98 (2005) 053514.
- [6] R. Menikoff, M.S. Shaw, The SURF model and the curvature effect for PBX 9502, *Combust. Theory Model.* 16 (2012) 1140–1169.
- [7] C. Handley, H.J. Lacy, B.D. Lambourn, N. Whitworth, H.R. James, CREST models for PBX 9501 and PBX 9502, in: *Fifteenth Symposium (Intl) on Detonation*, 2014, pp. 82–92.
- [8] A.K. Henrick, Shock-fitted numerical solutions of one- and two-dimensional detonation, PhD thesis, University of Notre Dame, 2008.
- [9] A.K. Henrick, T.D. Aslam, J.M. Powers, Simulations of pulsating one-dimensional detonations with true fifth order accuracy, *J. Comput. Phys.* 213 (2006) 311–329.
- [10] H.I. Lee, D.S. Stewart, Calculation of linear detonation instability: one-dimensional instability of plane detonation, *J. Fluid Mech.* 216 (1990) 103–132.
- [11] A.-R. Kasimov, D.-S. Stewart, On the dynamics of self-sustained one-dimensional detonations: a numerical study in the shock-attached frame, *Phys. Fluids* 16 (2004) 3566–3578.
- [12] H.D. Ng, A.J. Higgins, C.B. Kiyanda, M.I. Radulescu, J.H.S. Lee, K.R. Bates, N. Nikiforakis, Nonlinear dynamics and chaos analysis of one-dimensional pulsating detonations, *Combust. Theory Model.* 9 (2005) 159–170.
- [13] D.E. Lambert, D.S. Stewart, S. Yoo, B.L. Wescott, Experimental validation of detonation shock dynamics in condensed explosives, *J. Fluid Mech.* 546 (2006) 227–253.
- [14] T.D. Aslam, Shock temperature dependent rate law for plastic bonded explosives, *J. Appl. Phys.* 123 (2018) 145901.